POLITECNICO DI TORINO
Repository ISTITUZIONALE

Design and test of a parallel kinematic solar tracker

Original
Design and test of a parallel kinematic solar tracker / Mauro, Stefano; Battezzato, Alessandro; Biondi, Gabriele; Scarzella, Cristina. - In: ADVANCES IN MECHANICAL ENGINEERING. - ISSN 1687-8140. - 7:12(2015), pp. 1-16. [10.1177/1687814015618627]

Availability:
This version is available at: 11583/2625124 since: 2015-12-09T15:38:04Z

Publisher:
SAGE

Published
DOI:10.1177/1687814015618627

Terms of use:

This article is made available under terms and conditions as specified in the corresponding bibliographic description in the repository

Publisher copyright

(Article begins on next page)

01 September 2025

Research Article

Advances in Mechanical Engineering

Advances in Mechanical Engineering
2015, Vol. 7(12) 1–16
© The Author(s) 2015
DOI: 10.1177/1687814015618627
aime.sagepub.com
SAGE

Design and test of a parallel kinematic solar tracker

Stefano Mauro[1], Alessandro Battezzato[2], Gabriele Biondi[1] and Cristina Scarzella[1]

Abstract

This article proposes a parallel kinematic solar tracker designed for driving high-concentration photovoltaic modules. This kind of module produces energy only if they are oriented with misalignment errors lower than 0.4°. Generally, a parallel kinematic structure provides high stiffness and precision in positioning, so these features make this mechanism fit for the purpose. This article describes the work carried out to design a suitable parallel machine: an already existing architecture was chosen, and the geometrical parameters of the system were defined in order to obtain a workspace consistent with the requirements for sun tracking. Besides, an analysis of the singularities of the system was carried out. The method used for the singularity analysis revealed the existence of singularities which had not been previously identified for this kind of mechanism. From the analysis of the mechanism developed, very low nominal energy consumption and elevated stiffness were found. A small-scale prototype of the system was constructed for the first time. A control algorithm was also developed, implemented, and tested. Finally, experimental tests were carried out in order to verify the capability of the system of ensuring precise pointing. The tests have been considered passed as the system showed an orientation error lower than 0.4° during sun tracking.

Keywords

Kinematics, machine design, parallel mechanism, photovoltaics, robotics, singularity, solar energy

Date received: 23 April 2015; accepted: 24 September 2015

Academic Editor: Nima Mahmoodi

Introduction

Grid parity is a major issue in renewable energy systems (RES); it occurs when electricity generated by an alternative energy source is cheaper than purchasing power from the electricity grid. In order to reach grid parity, it is necessary to reduce the cost of energy production and to guarantee a high efficiency of the overall system. In photovoltaics, the degree of use and conversion of solar radiation directly affect the overall system efficiency. The quantity of exposed surface of the system and the comparison of the output energy produced with the input energy absorbed are the main elements to analyze. In Chin et al.[1] for instance, a single-axis smart sun tracker is developed to better direct the photovoltaic panels toward the sun in order to significantly increase the amount of energy produced. Concentrating the sunlight onto a very small high-efficiency solar cell[2–4] allows decreasing the influence of the cost of the solar cell on the cost of the total system[5] and a better rational use of the site of installation. Moreover, considering the same amount of output power, a concentrated system occupies less soil than a traditional one. The

[1]Department of Mechanical and Aerospace Engineering, Politecnico di Torino, Torino, Italy
[2]Istituto Italiano di Tecnologia, Torino, Italy

Corresponding author:
Stefano Mauro, Department of Mechanical and Aerospace Engineering, Politecnico di Torino, Corso Duca degli Abruzzi 24, 10129 Torino, Italy.
Email: stefano.mauro@polito.it

Creative Commons CC-BY: This article is distributed under the terms of the Creative Commons Attribution 3.0 License (http://www.creativecommons.org/licenses/by/3.0/) which permits any use, reproduction and distribution of the work without further permission provided the original work is attributed as specified on the SAGE and Open Access pages (https://us.sagepub.com/en-us/nam/open-access-at-sage).

Downloaded from ade.sagepub.com at Politecnico di Torino on December 9, 2015

concentration ratio[6] is a key factor in concentration photovoltaic (CPV) systems, and it has to be maximized in order to reach grid parity and higher efficiency. The precision requirement in the relative alignment between the sun and the system increases with the concentration ratio, as the acceptance angle of the system strongly decreases with this parameter. In high-concentration photovoltaic (HCPV) systems, the maximum allowed pointing error can decrease to 0.4°.

Among the trackers that are originally made to drive flat modules, only the ones that are characterized by a high precision in solar pointing and a high stiffness are suitable for the exploitation of the concentrator modules. In Roth et al.,[7] a powerful 2-degree-of-freedom (DOF) controlled architecture for sun tracking is illustrated. In Mousazadeh et al.,[8] a survey of the possible mechanism layouts for sun tracking is presented. This work shows that the most efficient device is the azimuth/elevation type: in Itul and Pisla[9] and Kulkarni et al.,[10] it is possible to find two examples of this type of device. Alignment errors are generally more effective on the energy production of concentrator modules. A misalignment larger than the acceptance angle causes a stop in energy production, whereas for a flat module it only causes a reduction in the power output. For that reason, the design of an efficient control system also seems to be important for maximum exploitation of an HCPV system.[11]

In the field of robotics, high stiffness requirements can often be addressed by adopting a parallel kinematic architecture.[12] This kind of mechanism is characterized by lower deflections of the limbs since the load is split between more links with respect to serial manipulators.

Many studies have dealt with the characterization of stiffness for parallel mechanisms in different applications.[13–15] The application of a suitable control technique makes it possible to obtain even higher precision.[16]

In particular, in the field of sun tracking, several different parallel mechanism layouts were proposed. A relevant example is provided in Cammarata.[17] In Alexandru and Pozna,[18] a two-axis solar tracker is deeply analyzed from the point of view of the dynamic deformation of the components of the mechanism under the force exerted by the wind. Some data about energy consumption for tracking are also reported. A high stiffness of the mechanism is gained through the usage of self-locking worm drives to actuate the joints. In Altuzarra et al.,[19] the sun tracking is pursued with a redundant 4-DOF parallel manipulator to reduce energy consumption. The kinematic design is presented, but no results are shown about the effective amount of absorbed energy. Besides, no results are presented regarding the stiffness of the manipulator. Moreover, it seems that a prototype has never been built.

As can be deduced by the state of the art,[20,21] parallel kinematic machines also show several disadvantages: their workspace is generally limited, and in some cases, it can be further limited by singularities. Moreover, the input–output relationship is generally highly nonlinear, making the control of the mechanism a delicate issue. The principal purpose of this article is then to completely develop a relevant example of a controlled parallel kinematic machine for sun tracking, trying to exploit the advantages of this kind of mechanism and limiting at the same time their well-known flaws.

This article describes the design process and the results obtained in the development of a solar tracker designed according to the layout proposed by Dunlop and Jones[22] and known as "the Canterbury tracker," consisting in a 3 RSR/US robot. This mechanism was originally devised for the purpose of night sky observation. Dunlop and Jones studied the kinematic properties of the mechanism from a theoretical point of view, and they extended their kinematic studies only to input/output singularities of the manipulator.

In this article, an analysis of the constraint singularities is also presented as a function of the different lengths of the links of the mechanism. Furthermore, the realization of a small-scale prototype and the tests performed to validate the suitability of the mechanism for sun tracking are described.

The first part of this work focuses on the problem of finding a geometrical configuration suitable to satisfy the workspace requirements to allow sun tracking in any season or latitude. The reachable configurations with different geometrical proportions are computed and singularities are analyzed. In this section, forward and inverse kinematics are also described.

The second part of this work deals with the construction of a small-scale prototype, its sensitization, and control in order to use the machine as a sun tracker. The developed control method uses an orientation sensor which was presented in Zeroual et al.,[23] while the control logic was specifically developed to deal with a parallel kinematic machine. Finally, the results of some tests carried out outdoors are presented and discussed.

Description of the structure

The mechanism driving the photovoltaic modules is presented herein and it is designed according to the schematics of Figure 1. It is a 2-DOF structure composed by two platforms linked by four limbs. Three of them are equal, and each one counts two identical bars (1) connected by a spherical joint (2) and attached to the fixed platform (3) and to the moving platform (4) by revolute joints (5). The hinges are located at the midpoints of the sides of two identical equilateral triangles, representing the platforms. The fourth limb (6) is fixed

Downloaded from ade.sagepub.com at Politecnico di Torino on December 9, 2015

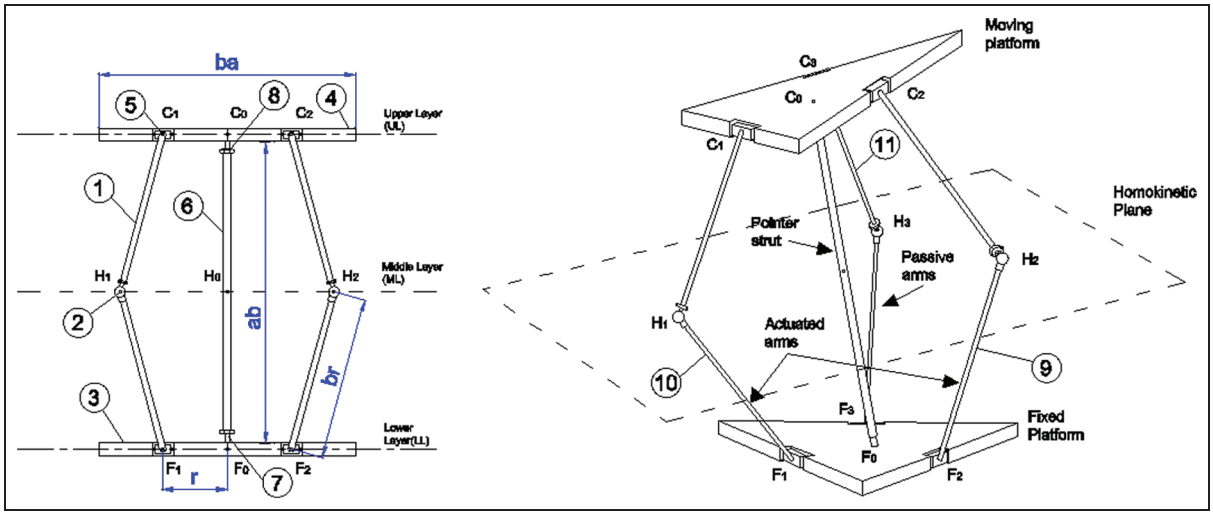

Figure 1. Parallel kinematic solar tracker: definition of the structure.

in the intersection of the bisectors of the angles of the same triangles.

The fourth limb, here called pointer strut, is attached to the center of both the fixed platform and the moving platform, respectively, by a spherical joint (7) and a universal joint (8). This inner limb is added in order to block the DOF along the vertical axis, keeping the centers of the two platforms always at the same distance one from another.

Photovoltaic modules are fastened to the moving platform. The azimuth and elevation angles are controlled by actuating two limbs (9, 10) while the third one is passive (11); the actuation elements are applied to the lower arms attached to the fixed platform.

Figure 2 shows the actuated angles β_1 and β_2; the azimuth (α) and elevation (ζ) angles define the orientation of the moving platform. The angles β_1 and β_2 are actuated through two stepper motors, to which a series of gear trains are linked to increase the output actuation torques. Each gear train is a self-locking worm drive. This means that the stiffness parameters associated with the actuated joints depend only on the warpage of the teeth under stress. The diagonal matrix composed by these *stiffness constants* is shown in the following equation:

$$\chi = \begin{bmatrix} 7.6 \times 10^6\,\mathrm{N\,m/rad} & 0 \\ 0 & 7.6 \times 10^6\,\mathrm{N\,m/rad} \end{bmatrix} \quad (1)$$

The values of the stiffness constants are evaluated from the information contained in datasheet of the worm drives. Any movement of the mechanism can be regarded, with a very good approximation, as a time sequence of static postures. This holds due to the nature of the stepper motors and the slowness of the motion. Indeed, during a minute the actuated angles have a nominal value variation that is equal to one-thousandth of a radiant as order of magnitude. For that reason, an analysis of the dynamics of the system becomes almost meaningless. On the contrary, a static stiffness analysis is useful to understand the order of magnitude of the external actions needed to provide unwanted displacements of the structure.

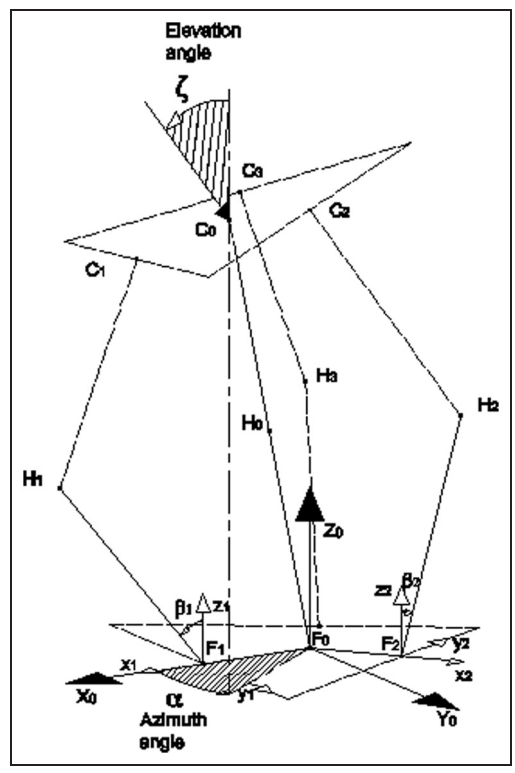

Figure 2. Solar angles related to the solar tracker and Cartesian coordinate systems.

Downloaded from ade.sagepub.com at Politecnico di Torino on December 9, 2015

Forward kinematics

The objective of this analysis is to define, for each configuration of the structure, where the photovoltaic panel is positioned subsequently to a command from the actuation system. Starting from the knowledge of the actuated angle, it is possible to solve a system of three equations (equation (2)) for determining the orientation of the pointer strut, which is directly related to the orientation of the moving platform.

The first of these equations derives from the fact that point H_0 (see Figure 1) is the middle point of the segment F_0C_0. The second and the third equations state that the pointer strut is always perpendicular to the two vectors connecting the midpoint of the pointer strut (H_0) and the centers of the spherical joints of the actuated limbs (H_1 and H_2), which lie in the π plane

$$\begin{cases} \left|\overrightarrow{F_0H_0}\right| = \frac{1}{2}\left|\overrightarrow{F_0C_0}\right| \\ \overrightarrow{F_0H_0}^T \cdot \overrightarrow{H_0H_1} = 0 \\ \overrightarrow{F_0H_0}^T \cdot \overrightarrow{H_0H_2} = 0 \end{cases} \tag{2}$$

The intersection of these equations leads to a quadratic equation for the third component H_{0z} of the position of point H_0 with respect to an inertial reference frame whose z-axis points toward the zenith, whose x-axis points south, and whose origin coincides with the center of the fixed platform

$$\begin{cases} rH_{0_z}^2 + wH_{0_z} + u = 0 \\ H_{0_x} = a_1H_{0_z} + a_2 \\ H_{0_y} = a_3H_{0_z} + a_4 \end{cases} \tag{3}$$

The coefficients in the set of equations (3) (r, w, u, a_1, a_2, a_3, and a_4) are not explicitly written for the sake of brevity, but they can be calculated starting from equation system 2 in a straightforward way. More details are provided in Mauro and Scarzella.[24] From the set of equations (3), it is possible to evaluate two different feasible positions of point H_0, from which four different couples of the values of the azimuth and the elevation angles are evaluable by means of the following obtainable relations

$$\begin{cases} \zeta = 2\cos^{-1}\left(\dfrac{2H_{0_z}}{\overline{ab}}\right) \\ \alpha = a\tan2\left(\dfrac{2H_{0_y}}{\overline{ab}\sin\left(\dfrac{\zeta}{2}\right)}, \dfrac{2H_{0_x}}{\overline{ab}\sin\left(\dfrac{\zeta}{2}\right)}\right) \end{cases} \tag{4}$$

in which $\overline{ab}$ is the length of the pointer strut.

However, for the concern of our device, only the values of the elevation angle included in a range from 0° to 90° are acceptable; other solutions should be discarded as they are not suited for sun tracking purpose. In particular, only one of the four couples satisfies the aforementioned condition.

Inverse kinematics

The elbows of each actuated arm follow a circular trajectory centered in the revolute joint; this trajectory intersects the π plane in two different points that are both possible positions of the elbow of the arm. The trajectory of the end of each actuated arm could be also represented as the intersection between a sphere centered in the ith revolute joint (the equation of the sphere is the first appearing in equation system (5)) and a plane perpendicular to the revolute joint axis and passing through the center of the joint. The components of the revolute joint axis are indicated with k_{ix}, k_{iy}, and k_{iz} in equation system (5).

The resultant circular trajectory is then intersected with the π plane, whose perpendicular vector is represented through its components π_x, π_y, and π_z. This last intersection is useful to evaluate the coordinates of the elbow of each actuated arm. After some considerations, the two actuated angles can be calculated. F_{ix}, F_{iy}, and F_{iz} and H_{ix}, H_{iy}, and H_{iz} in equation system (5), respectively, express the Euclidean coordinates of points F_i and H_i on the ith actuated limbs

$$\begin{cases} (x - F_{ix})^2 + (y - F_{iy})^2 + (z - F_{iz})^2 = \overline{br}^2 \\ k_{ix}(x - F_{ix}) + k_{iy}(y - F_{iy}) + k_{iz}(z - F_{iz}) = 0 \\ \pi_x(x - H_{ix}) + \pi_y(y - H_{iy}) + \pi_z(z - H_{iz}) = 0 \end{cases} \quad (i = 1, 2) \tag{5}$$

From the intersection of the three equations, it is possible to consider two quadratic and independent equations

$$\begin{cases} s_1H_{1_y}^2 + v_1H_{1_y} + t_1 = 0 \\ s_2H_{2_y}^2 + v_2H_{2_y} + t_2 = 0 \end{cases} \tag{6}$$

As for the solution of the forward kinematics, the coefficients of the quadratic equations are easily evaluable from equation system (5). Moreover, the x- and z-components of the position of points H_1 and H_2 are linear functions of components H_{1_y} and H_{2_y}, respectively.

So, two different possible positions for each point H_1 and H_2 can be found. The positions of these points correspond uniquely to a single value of each actuated angle. Then it is necessary to define a strategy to choose for each actuated angle the most convenient value between the two possible ones with the specified azimuth and elevation angles. In particular, the choice is done considering the current configuration of the actuators and so of the manipulator. At the beginning of each maneuver, the position and orientation of the

Downloaded from ade.sagepub.com at Politecnico di Torino on December 9, 2015

moving platform are characterized by an azimuth and an elevation angle, respectively, equal to 0° and 2°. In general, from the current configuration, the desired one is reached searching for the minimum feasible displacements and imposing four consecutive variations in the actuated angles.

Workspace and dimensions' definition

The workspace is defined as the set of positions that are reachable by the end-effector, which can be considered in this application as the photovoltaic panel mounted on the moving platform. Starting from the definition of workspace limits that are suitable for sun tracking, different dimensions of the various links were considered to determine the best geometric proportions for the mechanism, defined according to Figure 1. The boundaries of the workspace to be considered depend on the expected relative motion of the sun.

In order to generalize the analysis and to design a tracker that can work everywhere in the world, the following workspace limits have been fixed:

- Azimuth angle = [−180°; 180°];
- Elevation angle = [0°; 90°].

The geometrical parameters of the machine can be defined through two different geometrical ratios: the first is the ratio between the length $\overline{ab}$ of the strut and the length $\overline{br}$ of the arms of the articulated limbs; the second one is the ratio between the length $\overline{ba}$ of the side of the fixed platform profile and the length $\overline{br}$ of the arms. Having defined these parameters, it is possible to generate a heuristic procedure to find some optimal values for these ones. In particular, it has been considered that both ratios mentioned could vary between 0.5 and 2. If the ratios were out of this range, the resulting machine would have a very unbalanced structure with heavy movement difficulties. Then, a simple design of experiment table was generated: each of the ratios varies between its limits with a unit step equal to 0.25. Following this structure, a square grid of geometrical configurations of the mechanism is obtained. The geometrical configurations considered are totally 49, which correspond to 49 different experiments. Each experiment consists of the calculation of the azimuth and elevation angles corresponding to a finite set of couples of joint angles. The calculation is made by solving the forward kinematics of the mechanism. For each experiment, each of the two actuated angles varies between −30° and 125° with a unit step of 1°. This means that the total number of times in which the forward kinematic of the machine is solved is 156^2 per experiment, for a total number of $156^2 \times 49$ calculations.

It should be noted that to be more efficient from a computational point of view, a Monte Carlo method could have been applied. However, the method used was not excessively heavy and all the experiments were completed within a short time.

For each experiment, the 156^2 possible configurations of the machine correspond to an equal number of pairs of orientation angles (azimuth and elevation) of the moving platform. They define a portion of a rectangular surface whose sides are defined by the aforementioned workspace limits. The ratio between the found portion and the entire rectangular area is a parameter quantifying the optimality of the geometric pattern corresponding to the experiment. Figure 3 shows the portions associated with three different geometric conditions of the manipulator: on the left side, both the arm and the side of the platform have a length that is equal to the double of the pointer strut length (both ratios are equal to 0.5), while on the right side the length of the side of the platform is doubled (the first ratio remains equal to 0.5 while the other becomes 1).

In both cases, the geometry of the workspace is comparable to two bell-shaped surfaces. Moreover, the ratio between the portion dimension and the total surface of the workspace is less than 0.5. This means that those geometric proportions are not suitable for sun tracking because the tracker cannot cover certain areas included in the fixed workspace boundaries.

The map in the bottom of Figure 3 is found imposing instead the length of the pointer strut and the length of the side, respectively, equal to 0.8 and 0.6 times the length of the arms; in this condition, the workspace is quasi-completely covered. The value of the ratio between the covered portion and the total surface is 0.91. This is the highest value among those found following the generated design of experiment table. For that reason, the aforementioned proportions were considered optimal to build the prototype of the machine. In order to check the actual functionality of the machine, further analyses were carried out to exclude the presence of kinematic singularities within the covered workspace.

Singularity analysis

In general, singular configurations of a mechanical system are particular states where the DOFs of the mechanism change instantaneously; if unpredicted, they could become un-desirable configurations. In particular, when a mechanism is in a singular configuration, the pose of its end-effector instantaneously loses controllability.

For instance, it can occur that the end-effector gets some virtual displacement even considering all the actuators blocked. In this condition, the system

Downloaded from ade.sagepub.com at Politecnico di Torino on December 9, 2015

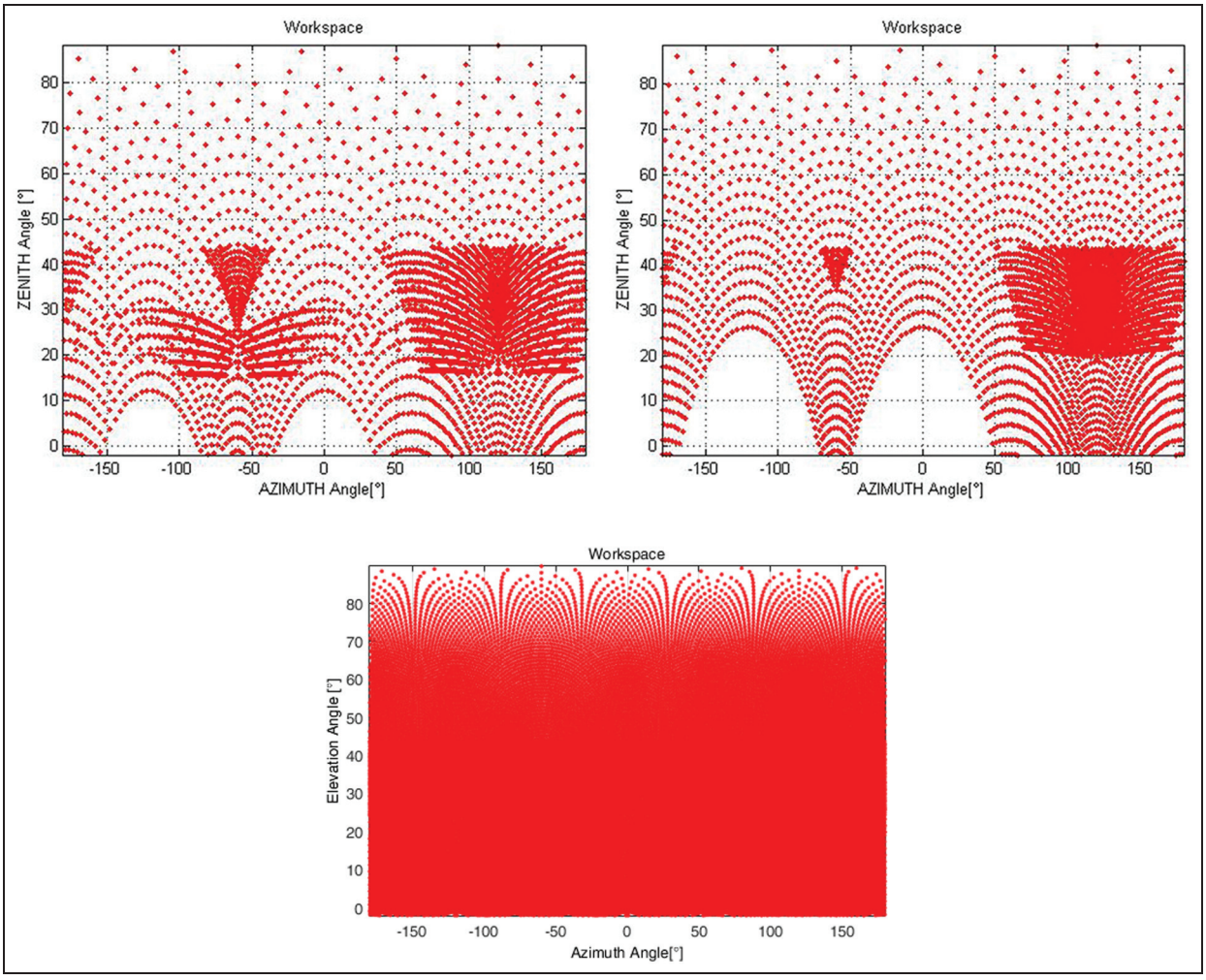

Figure 3. Feasible end-effector positions (marked with red points). Upper-left ratios: 0.5–0.5; upper-right ratios: 0.5–1; bottom ratios: 0.8–0.6.

becomes uncontrolled, so it is fundamental to predict in which configurations this happens. In that sense, the singularity analysis is essential for design and control purposes and has drawn considerable attentions. In general, a closed-loop kinematic chain can be considered as a set of rigid bodies connected to each other by mechanical joints. Some of these joints can be actuated so that it is possible to define some variables that describe the feasible displacements given by the joints. The set of all possible values of these input variables defines the so-called input space or joint space. At the same time, it is possible to choose a group of variables that describe the motion of a particular point of the structure. Similarly, the set of all feasible values of these output variables defines the so-called output space or workspace.

Considering a spatial parallel mechanism, it is common to choose as output variables six parameters that fully represent the position and the attitude of the end-effector, which is often a moving platform connected to several limbs. An appropriate choice of the parameters leads, in particular, to obtain that the derivatives of the output variables are those shown in the vector

$$\$_p = \begin{bmatrix} \bar{\omega} \\ \bar{v}_O \end{bmatrix} \tag{7}$$

where $\bar{\omega}$ is the absolute angular velocity of the moving platform and $\bar{v}_O$ is the linear velocity of a point linked to the moving platform and instantaneously coincident with the origin of the coordinate system in which the vector is expressed. This vector $\$_p$, which completely describes the instantaneous motion of the moving platform, may be considered as a linear combination of l_i *unit twists*, l_i being the number of 1 d.o.f joints of a generic ith limb of the manipulator (of which only g_i are actuated). A unit twist is considered as a mathematical representation of a motion of the limb which is feasible with one of its joints. In general, a number of

Downloaded from ade.sagepub.com at Politecnico di Torino on December 9, 2015

$6-(l_i-g_i)$ *constraints* on the limb passive motion should exist. A mathematical representation of these constraints is given by a set of so-called *unit wrenches*, whose orthogonal product with the twist associated with passive joints of the limb is null (these twists and wrenches are considered as *reciprocal screws*).[25] When this set is identified for each limb of the mechanism, it is possible to write a compact equation that fully describes the mapping between the joint space and the workspace

$$J_x \$_p = J_q \dot{\bar{q}} \tag{8}$$

where $\dot{\bar{q}}$ is the vector of the derivatives of the input variables.

When this mapping is singular, as it occurs when J_x, J_q, or both are not full-rank matrices, the number of DOFs of the manipulator changes instantaneously. In particular, when J_x is not full-rank, the mechanism gains at least one uncontrollable DOF, or in other words the mechanism can have a movement while all actuators are locked. This dangerous condition is acknowledged as *forward kinematic singularity*. Otherwise, when J_q has null rows or columns, the mechanism loses DOFs; in other words, the end-effector cannot move along certain directions. This situation is classified as an *inverse kinematic singularity*. When both J_x and J_q present null rows or columns for the same configuration, a so-called *C-space singularity* occurs: in that case, both previously examined behaviors can occur.

These singularities analyzed are cataloged as *input–output singularities*, and they strictly depend on the choice of the input and output variables. In general, another kind of singularity can be found which does not depend on this choice, but that depends on the mechanical structure of the manipulator: a *constraint singularity*.[26]

Considering all the joints of the mechanism as passive joints, one can observe that it is generally possible to find a number of $6-l_i$ linearly independent unit wrenches for each ith limb of the mechanism which are reciprocal to all twists representing the motion of each joint of the ith limb. A global set of constraints for the moving platform are then definable which define at the same time their DOFs. Given a number h of constraints, each represented by a unit wrench $\hat{\$}_{r_{i,k}}$, the number of DOFs of the moving platform should be $M=6-h$ if they are all linearly independent. However, as unit wrenches depend on the particular configuration of the mechanism, there could be some configurations in which they are not linearly independent, and this should involve an instantaneous change in the number of DOFs of the platform. In this context, a matrix J_c is definable as follows

$$J_c = \begin{bmatrix} \hat{\$}^T_{r_{1,1}} \\ \vdots \\ \hat{\$}^T_{r_{1,6-l_1}} \\ \hat{\$}^T_{r_{2,1}} \\ \vdots \\ \hat{\$}^T_{r_{2,6-l_2}} \\ \vdots \\ \hat{\$}^T_{r_{m,1}} \\ \hat{\$}^T_{r_{m,6-l_m}} \end{bmatrix} \tag{9}$$

When J_c is not full-rank, the moving platform gains at least one supplementary DOF. The mechanism represented in Figure 1 has four limbs: three of them are RSR chains and the last one is a passive US chain. In particular, only the first two of the RSR chains have one actuated joint while the third one is completely passive. Considering Figure 1, the vectors $\bar{c}_i = C_i - C_0$, $\bar{a}_i = H_i - F_i$, and $\bar{b}_i = C_i - H_i$ can be defined for each RSR chain, which has five DOFs. So five unit twists describe the instantaneous displacements that are feasible with joints. Indicating with $\hat{s}_{1i}$ and $\hat{s}_{5i}$ the axes of the bottom and top revolute joints for each limb, three independent rotation axes passing through the center of each spherical joint can be found: $\hat{s}_{2i} = \hat{s}_{1i}$, $\hat{s}_{3i} = \hat{a}_i$, and finally $\hat{s}_{4i} = \hat{s}_{2i} \times \hat{s}_{3i}$. Then three sets of unit twists are definable for $i = 1, 2, 3$ (one for each limb)

$$\hat{\$}_{1,i} = \begin{bmatrix} \hat{s}_{1i} \\ (\bar{c}_i - \bar{b}_i - \bar{a}_i) \times \hat{s}_{1i} \end{bmatrix}, \hat{\$}_{2,i} = \begin{bmatrix} \hat{s}_{2i} \\ (\bar{c}_i - \bar{b}_i) \times \hat{s}_{2i} \end{bmatrix},$$
$$\hat{\$}_{3,i} = \begin{bmatrix} \hat{s}_{3i} \\ (\bar{c}_i - \bar{b}_i) \times \hat{s}_{3i} \end{bmatrix}$$
$$\hat{\$}_{4,i} = \begin{bmatrix} \hat{s}_{4i} \\ (\bar{c}_i - \bar{b}_i) \times \hat{s}_{4i} \end{bmatrix}, \hat{\$}_{5,i} = \begin{bmatrix} \hat{s}_{5i} \\ \bar{b}_i \times \hat{s}_{5i} \end{bmatrix} \tag{10}$$

In particular, point C_0 was selected as the origin of the reference frame of the unit twists. Since the DOFs of this kind of chain are 5, only one unit wrench exists which is reciprocal to all twists. This must be a pure force which is constrained to lie on the plane defined by the center of the spherical joint and the $\hat{s}_{1i}$ axis and also on the plane defined by the joint center and the $\hat{s}_{5i}$ axis.

So, being $\hat{n}_{a_i} = \hat{s}_{1i} \times \hat{a}_i$ and $\hat{n}_{b_i} = \hat{s}_{5i} \times \hat{b}_i$, it is

$$\hat{\$}_{r_{i,1}} = \begin{bmatrix} \hat{n}_{a_i} \times \hat{n}_{b_i} \\ (\bar{c}_i - \bar{b}_i) \times (\hat{n}_{a_i} \times \hat{n}_{b_i}) \end{bmatrix} \tag{11}$$

A visualization of this statement is shown in Figure 4.

The fourth limb is composed by a universal and a spherical joint, so it has 5 DOFs. Considering all the feasible displacements with these joints, a unique

Downloaded from ade.sagepub.com at Politecnico di Torino on December 9, 2015

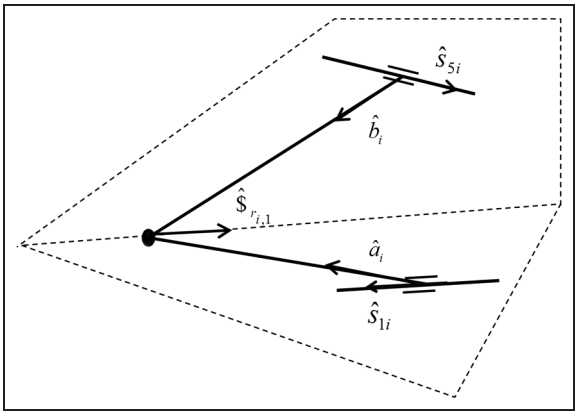

Figure 4. Reciprocal wrench to all virtual displacements of the RSR chains.

wrench which does not exert virtual work along these displacements must be a pure force that passes through both centers of the joints. $\hat{s}_4$ being the direction of the vector $C_0 - F_0$, the expression of this wrench is

$$\hat{\$}_{r_{4,1}} = \begin{bmatrix} \hat{s}_4 \\ \bar{0} \end{bmatrix} \tag{12}$$

Figure 5 shows this concept.

The 4×6 matrix J_c is fully defined considering equations (11) and (12)

$$J_c = \begin{bmatrix} \left((\bar{c}_1 - \bar{b}_1) \times (\hat{n}_{a_1} \times \hat{n}_{b_1})\right)^T & (\hat{n}_{a_1} \times \hat{n}_{b_1})^T \\ \left((\bar{c}_2 - \bar{b}_2) \times (\hat{n}_{a_2} \times \hat{n}_{b_2})\right)^T & (\hat{n}_{a_2} \times \hat{n}_{b_2})^T \\ \left((\bar{c}_3 - \bar{b}_3) \times (\hat{n}_{a_3} \times \hat{n}_{b_3})\right)^T & (\hat{n}_{a_3} \times \hat{n}_{b_3})^T \\ \bar{0}^T & \hat{s}_4^T \end{bmatrix} \tag{13}$$

Once matrix J_c is defined, it is appropriate to identify an input–output relationship in the form of equation (8). Considering the two RSR chains that have the first joint actuated, one can identify for each limb a set of wrenches that must be reciprocal to all twists considered in equation (10), excluding $\hat{\$}_{1,i}$ that is associated with the actuated joint. This can be done in order to eliminate the contribution of the passive joints to the instantaneous motion of the end-effector. The exclusion of the actuated joint leads to consider the joint itself as locked. This means in other words that the limb is constrained to have only 4 DOFs. So, there will be two linearly independent wrenches (constraints) that are reciprocal to the four twists representing the DOFs. These two wrenches can be chosen arbitrarily between those lying in the plane defined by the passive revolute joint axis and the center of the spherical joint. An illustration of that can be seen in Figure 6.

To eliminate the contribution of passive joints to the motion of the platform, any of the aforementioned reciprocal wrenches can be chosen. The chosen wrench can be multiplied then by each member of equation (8).

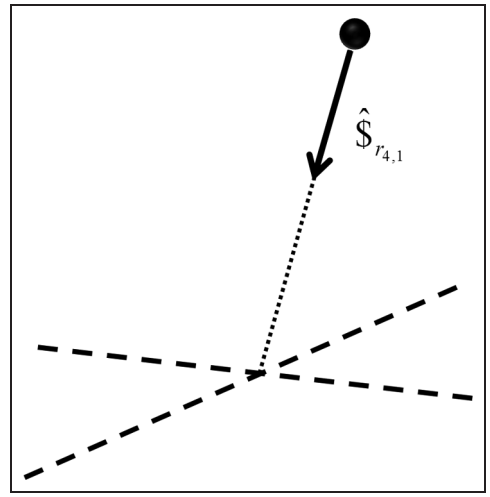

Figure 5. Reciprocal wrench to all virtual displacements of the pointer strut.

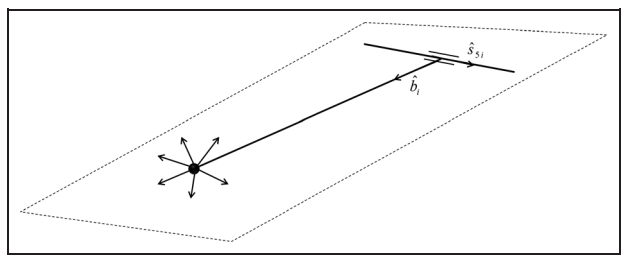

Figure 6. Reciprocal wrenches to twists associated with the passive joints of the actuated RSR chains.

A possible choice for each actuated limb can be for instance

$$\hat{\$}^*_{r_{i,1}} = \begin{bmatrix} \hat{s}_{1_i} \times \hat{n}_{b_i} \\ (\bar{c}_i - \bar{b}_i) \times (\hat{s}_{1_i} \times \hat{n}_{b_i}) \end{bmatrix} \tag{14}$$

This choice leads to

$$\hat{\$}^*_{r_{i,1}} \$_p = -\dot{q}_{1,i} |\bar{a}_i| (\hat{n}_{a_i} \times \hat{n}_{b_i}) \cdot \hat{s}_{1_i} \tag{15}$$

Hence, the 2×6 J_x and the 2×2 J_q matrices can be made explicit through

$$J_x = \begin{bmatrix} \left((\bar{c}_1 - \bar{b}_1) \times (\hat{s}_{1_1} \times \hat{n}_{b_i})\right)^T & (\hat{s}_{1_1} \times \hat{n}_{b_1})^T \\ \left((\bar{c}_2 - \bar{b}_2) \times (\hat{s}_{1_2} \times \hat{n}_{b_2})\right)^T & (\hat{s}_{1_i} \times \hat{n}_{b_2})^T \end{bmatrix} \tag{16}$$

$$J_q = \begin{bmatrix} -|\bar{a}_1| (\hat{n}_{a_1} \times \hat{n}_{b_1}) \cdot \hat{s}_{1_1} & 0 \\ 0 & -|\bar{a}_2| (\hat{n}_{a_2} \times \hat{n}_{b_2}) \cdot \hat{s}_{1_2} \end{bmatrix} \tag{17}$$

Clearly, these matrices depend on the particular choice of the wrenches, but it is fundamental to understand that when the manipulator is under a singular configuration the matrices will be rank-deficient with any choice of the wrenches. Coherently, when the

Downloaded from ade.sagepub.com at Politecnico di Torino on December 9, 2015

mechanism is not under a singular configuration, any choice of the wrenches will produce full-rank matrices. In detail, an inverse kinematic singularity will occur when every selectable wrench for one of the limbs is reciprocal to the twist associated with the actuated joint. This obviously occurs when the limb is completely stretched out or folded back. There is no other configuration in the considered mechanism that can cause a loss of instantaneous mobility. All the inverse kinematic singularities of the mechanism are associated with the boundary of the workspace.

As regards the forward kinematics singularities, they can occur only in the case of parallelism between the vectors $C_2 - H_2$ and $C_1 - H_1$; otherwise, the selectable wrenches are not coplanar. However, in this condition J_x becomes a null matrix and equation (8) degenerates; in this condition, a C-space singularity occurs.

From these considerations, it emerges that the input–output relationship does not provide interesting information in the context of the singularity analysis, but the analysis of constraint singularities remains fundamental.

In order to make the analysis, simulations have been performed compiling a MATLAB code which performs the singular value decomposition (SVD) of the J_c matrix and evaluates the conditions in which that matrix is near to be rank-deficient (high conditioning number).

During the year, the sun apparently performs a path on a portion of the sky which can be delimited by the following angular ranges:

- Elevation angle range: [0°; 90°];
- Azimuth angle range: [−120°; 120°].

With the purpose of obtaining the limits of the workspace of the mechanism, the simulations have been performed extending the ranges up to [−180°; 180°]. Figure 7 shows with " + " markers the configurations of the mechanism in which a constraint singularity occurs. The portion of the workspace useful for the tracking purpose is singularity-free. The blue areas represent all the configurations that are impossible for the spatial mover. Then it is possible to state that the chosen geometric characteristics of the manipulator are feasible with the tracking purpose.

Nominal stiffness properties and energy consumption

For a parallel manipulator, the joint displacement Δq is related to the end-effector deflection Δx by the conventional Jacobian matrix J

$$\Delta q = J\Delta x \tag{18}$$

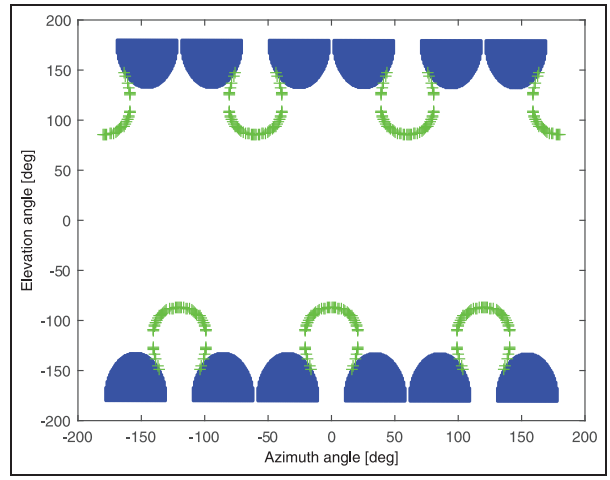

Figure 7. Constraint singularities and workspace boundaries.

where $J = J_q^{-1}J_x$. As the external forces are linearly related to the displacements in general, it is possible to write

$$F = K\Delta x \tag{19}$$

where K is a symmetric, positive semi-definite matrix. If the links of the mechanism are considered non-deformable, this *stiffness matrix* is only dependent on the stiffness constants of the joints and the configuration of the mechanism. Indeed, the joint displacement is caused by deflection torques τ applied on the gear motors. Hence

$$\tau = \chi\Delta q \tag{20}$$

Moreover, it holds that

$$F = J^T\tau \tag{21}$$

From equations (19–21) the following relationship could be obtained

$$K = J^T\chi J \tag{22}$$

From the last equation, the dependencies of the stiffness matrix are easily deduced. Therefore, the stiffness matrix of the designed mechanism can be calculated for some particular configurations of the mechanism designed. For instance, it is possible to consider two sun tracking maneuvers in two extremely different conditions. In particular, the nominal apparent trajectory of the sun during the two solstices can be evaluated. Solving the inverse kinematics of the machine, it is at the same time possible to consider the time evolution of the complete pose of the mechanism, or in other words, it is possible to compute the Jacobian matrix in different instants of time. This allows the direct evaluation of matrix K. In particular, it is possible to find the worst configuration for the stiffness of the mechanism

Downloaded from ade.sagepub.com at Politecnico di Torino on December 9, 2015

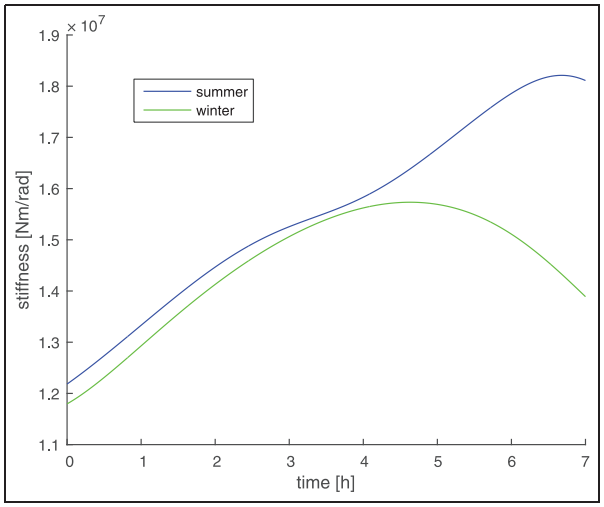

Figure 8. Time behavior of the minimum between the two non-null eigenvalues of the stiffness matrix.

examining the behavior of the minimum non-null eigenvalue of matrix K. In Figure 8, the minimum eigenvalue of K is represented as a function of time and the maneuver. The blue line is relative to sun tracking during the summer solstice and the green one is relative to sun tracking during the winter solstice.

The entire stiffness matrix corresponding to the worst condition for the mechanism is shown in equation (23) at the bottom of the page.

Considering, for instance, the following end-effector deflection (deflections in the platform orientation are represented with fixed-axis 123 Euler angles)

$$\Delta x^* = \begin{bmatrix} 0.1\,\text{mm} \\ 0.1\,\text{mm} \\ 0.1\,\text{mm} \\ 0.3^\circ \\ 0.3^\circ \\ 0.3^\circ \end{bmatrix} \tag{24}$$

The corresponding external wrench is

$$F^* = \begin{bmatrix} 1.66\,\text{kN} \\ -9.18\,\text{kN} \\ 1.92\,\text{kN} \\ -30\,\text{kN m} \\ 27.7\,\text{kN m} \\ 21.2\,\text{kN m} \end{bmatrix} \tag{25}$$

which apparently is a quantity that cannot be exerted by any regular natural agent. In fact, considering that the surface of the moved PV module is $0.36\,\text{m}^2$, the maximum force exerted by wind at 30 m/s has a magnitude of 360 N.

Another interesting analysis that can be done is relative to the mechanical work needed to perform the two considered extreme maneuvers. This analysis can be pursued exploiting equation (21) through the inversion of the transpose of the conventional Jacobian matrix J. Once the joint forces τ are evaluated, the mechanical work can be computed according to its definition, considering the efficiency of the gear trains equal to 0.59 (the trajectory in the input space was already evaluated during the former stiffness analysis).

In general, the nominal exerted wrench on the end-effector (neglecting the weight of the limbs) of the mechanism is

$$F_{nom} = \begin{bmatrix} 0 \\ 0 \\ -gm \\ 0 \\ 0 \\ 0 \end{bmatrix} \tag{26}$$

g being the gravity acceleration and m the carried payload (10 kg).

The required joint torques are represented by two charts in Figure 9. The total required daily work during the winter solstice is 23.3 J, while during the summer solstice it is 22.1 J. It is important to note that the duration of the day during summer is definitively longer in Turin.

These values are actually low, even considering that they are referred to a small-scale prototype. In order to compare power consumption with the expected power production, it should be considered that the payload is compatible with a 0.36-m^2 high-concentration module, with a peak power of about $108\,\text{W}_\text{p}$. The expected daily production can be estimated as 1.5 MJ. So, the nominal spending in terms of work for the movement of the machine is completely negligible with respect to the produced energy. Moreover, these values are much lower than those found by Alexandru and Pozna.[18]

$$K^* = \begin{bmatrix} 0.115\,\text{N/m} & -0.106\,\text{N/m} & 0.073\,\text{N/m} & -0.128\,\text{N/rad} & -0.154\,\text{N/rad} & 0.312\,\text{N/rad} \\ -0.106\,\text{N/m} & 0.155\,\text{N/m} & -0.073\,\text{N/m} & 0.321\,\text{N/rad} & -0.084\,\text{N/rad} & -0.412\,\text{N/rad} \\ 0.073\,\text{N/m} & -0.073\,\text{N/m} & 0.0471\,\text{N/m} & -0.104\,\text{N/rad} & -0.072\,\text{N/rad} & 0.212\,\text{N/rad} \\ -0.128\,\text{N/rad} & 0.321\,\text{N/rad} & -0.104\,\text{N/rad} & 0.866\,\text{N m/rad} & -0.629\,\text{N m/rad} & -0.793\,\text{N m/rad} \\ -0.154\,\text{N/rad} & -0.084\,\text{N/rad} & -0.072\,\text{N/rad} & -0.629\,\text{N m/rad} & 1.091\,\text{N m/rad} & 0.075\,\text{N m/rad} \\ 0.312\,\text{N/rad} & -0.412\,\text{N/rad} & 0.212\,\text{N/rad} & -0.793\,\text{N m/rad} & 0.075\,\text{N m/rad} & 1.121\,\text{N m/rad} \end{bmatrix} \cdot 10^7 \tag{23}$$

Downloaded from ade.sagepub.com at Politecnico di Torino on December 9, 2015

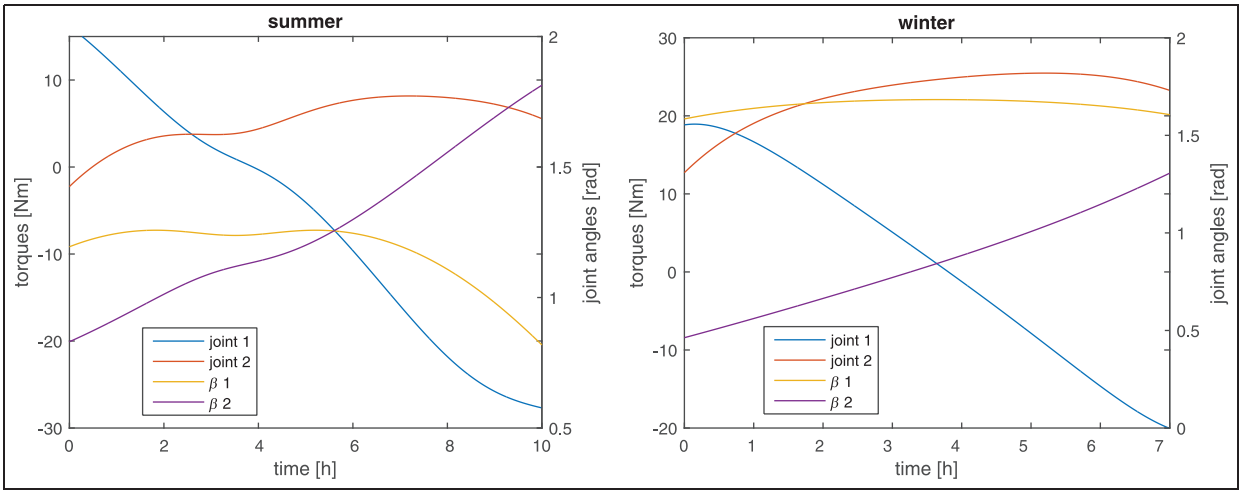

Figure 9. Actuated joint positions for sun tracking with corresponding required joint torques: on the left the date is 21 June 2014; on the right it is 21 January 2014.

Prototype design and construction

In order to design and build a prototype, a payload of 10 kg was considered, including the sensors and a test concentration module (0.36 m^2). At the same time, it has been evaluated that commercially available high-concentration modules equipped with secondary lens allow an acceptance angle of 0.4°.

The mechanical solution used to build a mechanism that corresponds to the analyzed kinematic scheme is described as follows. In order to obtain a large range of angular motion, the spherical joints of the external limbs were built according to the roll–bend–roll schematics. The spherical joint of the point strut requires a free relative motion within a cone of amplitude equal to 90°. For this reason, it was built by assembling a universal joint and a revolute joint.

The whole tracker also includes six revolute joints; they connect the fixed and the moving platform to the three RSR chains. To guarantee these mechanical couplings, a connection element has been designed to obtain the coupling by an interference clamping and a pin. This element includes two seats: one for the tubular part of the kinematic chain and the other for a connection shaft. Considering that two revolute joints are actuated, they have a keyway for a flat key in charge to ensure a regular torque transmission.

The pointer strut imposes the spherical trajectory to the moving platform and fixes the height of the structure; therefore, it guarantees the correct sun tracking. The strut is composed of a central tubular element connecting two universal joints which engage in the two platforms by means of supports. The lower one is then assembled on a revolute joint that allows a rotation around the vertical axis. Figure 10 shows the prototype and a detail of the anchoring points of the limbs with the moving platform.

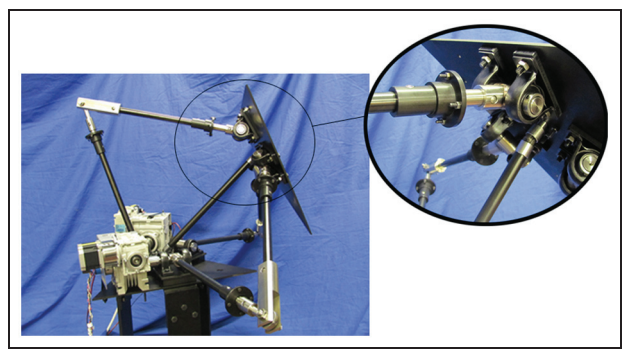

Figure 10. Prototype of the parallel kinematic solar tracker.

Actuation system and sensors

Two stepper motors have been chosen to power the tracker: they are commonly used for position control applications because of their properties of load independence, good holding torque, and excellent response time. Each stepper motor has got a step angle of 1.8°, and it can be driven with a quarter step precision, that means 0.45°. In order to contain the dimensions of the actuation system, increasing the torque and reducing the step angle at the same time, a gear train (600:1) has been coupled to each motor. The position of each actuated kinematic chain is measured by two rotary potentiometers placed on the same axes of the motors. The orientation toward the sun is detected by an orientation sensor. This mainly consists of four photodiodes displaced in a plane and separated by two orthogonal opaque walls with an upper screen whose geometry has been calculated in order to let all the photodiodes to be enlightened as far as the alignment error is lower than 0.35°. This last sensor is used to provide feedback to the closed-loop control in order to reach high pointing

Downloaded from ade.sagepub.com at Politecnico di Torino on December 9, 2015

Table 1. Association between photodiodes signals and motion direction.

PH_1	Off	Off	Off	Off	Off	Off	Off	Off	On	On	On	On	On	On	On
PH_2	Off	Off	Off	Off	On	On	On	On	Off	Off	Off	On	On	On	On
PH_3	Off	Off	On	On	Off	Off	On	On	Off	On	On	Off	Off	On	On
PH_4	Off	On	Off	On	Off	On	Off	On	On	Off	On	Off	On	Off	On
$\Delta\alpha$	–	$+\Delta$	$+\Delta$	$+\Delta$	$-\Delta$	NA	$-\Delta$	NA	$+\Delta$	NA	NA	0	NA	NA	0
$\Delta\zeta$	–	$+\Delta$	$-\Delta$	0	$-\Delta$	NA	0	NA	0	NA	NA	$-\Delta$	NA	NA	0

NA: not available.

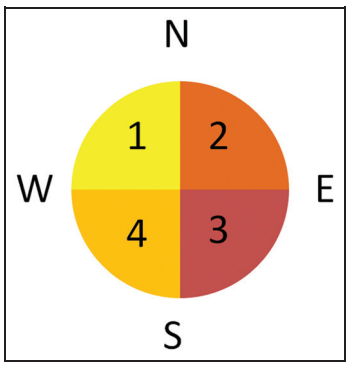

Figure 11. Photodiode codes.

precision. It is important to note that the final purpose of the mechanism is to provide continuously the maximum amount of solar energy obtainable from the high-concentration photovoltaic modules carried by the mechanism. This maximum amount is obtained in a given infinitesimal instant of time if and only if the alignment error in the instant is lower than 0.4°. On the contrary, if the error was larger than this threshold, the production would drop to 0. So the main parameter that should be examined to understand whether the requirements are fulfilled is the percentage of the total operation time in which the sensor is completely enlightened. If this percentage is near to 100, it means that the system is absolutely optimal for the purpose of sun tracking.

Voltage signals coming from the photodiodes are converted into digital signals: when the voltage is higher than a fixed threshold, the value of a Boolean variable is set to 1; otherwise, it is set to 0. If all values are set to 1, the end-effector of the mechanism is accurately directed toward the sun location. If this does not occur, an embedded control system manages to reposition the moving platform. To reach this goal, the control logic is based on a decision map (Table 1) that analyses the four Boolean signals coming from the orientation sensors and decides the direction of the motion of tracker.

The sensors are numbered according to the schematics of Figure 11. If they all are on, the system is aligned; otherwise, it must move in order to recover alignment. In that case, the mechanism is driven to perform step motion of constant amplitude Δ along the azimuth (α) and/or elevation (ζ) direction. Table 1 is a map to decide whether the system must move along azimuth or elevation direction, or along them both, and in which sense, depending on which photodiodes are enlightened.

The lines marked with labels PH_i indicate the value of the Boolean associated with signal from the *i*th photodiode. The lines marked $\Delta\alpha$ and $\Delta\zeta$ indicate the required motion along azimuth and elevation, respectively. $+\Delta$ means a positive step and $-\Delta$ a negative one. As some signal combinations are not suitable, they should not be found during operations. Hence, in those cases, the "NA" label is reported in the table. In order to point the mechanism toward the sun, the control schematic of Figure 12 is applied.

In any time instant, the actual position of the mechanism is detected by the potentiometers that measure the angular position of the actuated limbs (β_1 and β_2). At the same time, the photodiodes provide signals useful to evaluate whether the system is pointing the sun or, otherwise, in which direction it must move.

The photodiode signal processing software module applies the rules of Table 1 and computes the motion required along azimuth ($\Delta\alpha$) and elevation ($\Delta\zeta$). The direct kinematic software module computes the current azimuth (α) and elevation (ζ) angles. The motion required is then summed to the current position in order to obtain a couple of updated reference values for azimuth and elevation angles (α_{ref} and ζ_{ref}). The reverse kinematic software module computes the updated reference values for the angles of the actuated limbs $\beta_{1,ref}$ and $\beta_{2,ref}$. Finally, the number of steps for the motors is computed considering the difference between the reference values and the actual values of angles β_1 and β_2. These values are the inputs for the motor drivers. The control loop is applied all day long, so it recovers the misalignment that periodically occurs because of the sun apparent motion.

Tests

Test setup

The first tests were carried out in order to verify the system capability to point toward the sun according to

Downloaded from ade.sagepub.com at Politecnico di Torino on December 9, 2015

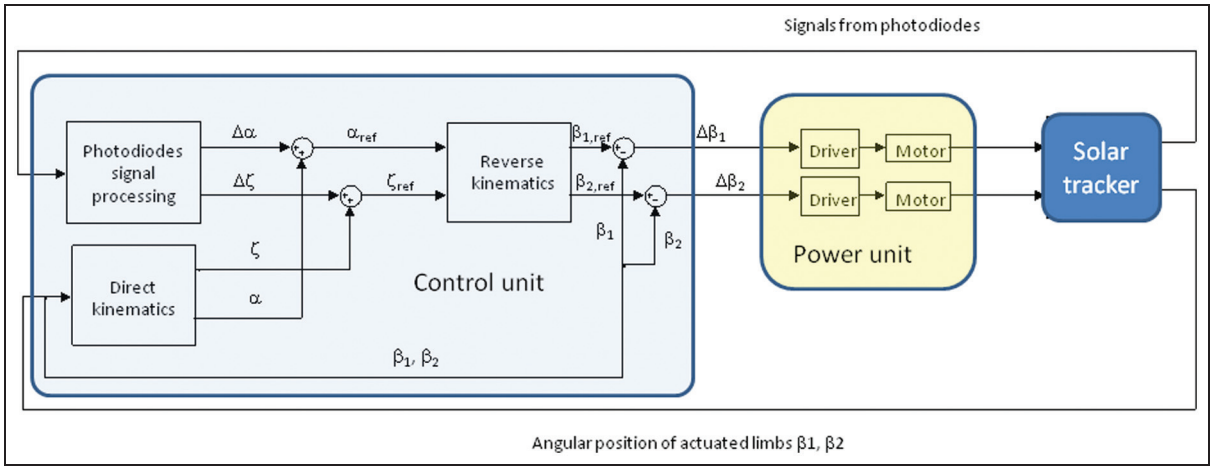

Figure 12. Control schematic.

the alignment error detected by the photodiode sensor (0.35°). The test setup includes a computer used for real-time control and a second one for data acquisition purpose.

The control computer is connected to the sensors used in the control algorithm, that is, the photodiodes of the orientation sensor and the potentiometers that detect the angular position of the actuated limbs. It also provides the commands to the machine motors.

The data acquisition computer records data from the machine sensors, the commands sent to the motors, and the signal provided by a pyranometer fixed with the moving platform. In order to continuously check the alignment, the pyranometer was masked in such a way to be enlightened only if it is aligned toward the sun with an alignment error lower than 0.4°. So, this signal is proportional to the solar radiation when the tracker alignment is lower than 0.4°; otherwise, it drops to 0.

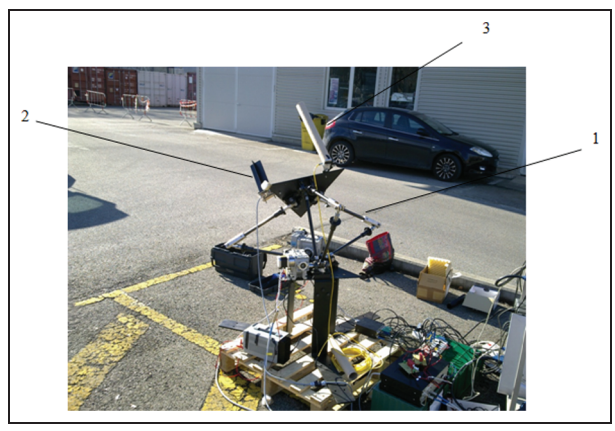

Figure 13. Test setup: 1, sun tracker prototype; 2, orientation sensor; 3, masked pyranometer.

Test results

Figure 13 shows the system during tests. The sun tracker (1), the orientation sensor (2), and the masked pyranometer (3) can be seen. Control and data acquisition computers are on the right.

Figure 14 shows the history of the signal provided by each photodiode during an alignment transient. It can be noted that all the sensors reached the "high" state for t = 25 s. This means that after that time the tracker was aligned with the sun direction and the motors were stopped. The differences between the signals coming from the photodiodes are due to the slight physical diversities of the various electronic components of the sensors and to residual errors.

The chart in Figure 15 illustrates the time history of the signal from photodiodes PH_{1-4} during a tracking phase of 2000 s. They can be distinguished between

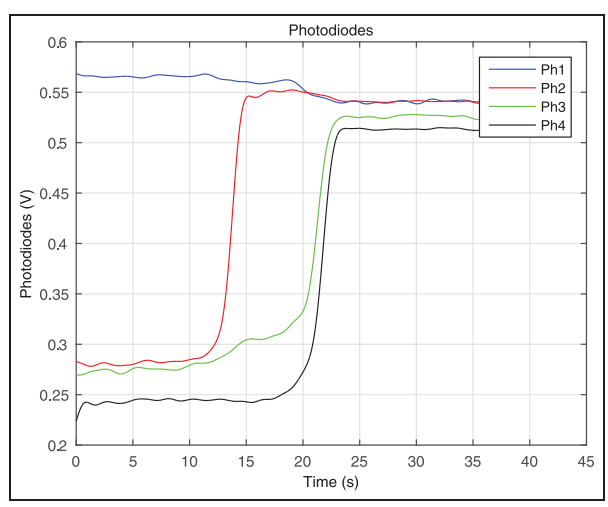

Figure 14. Photodiodes during the active tracking.

Downloaded from ade.sagepub.com at Politecnico di Torino on December 9, 2015

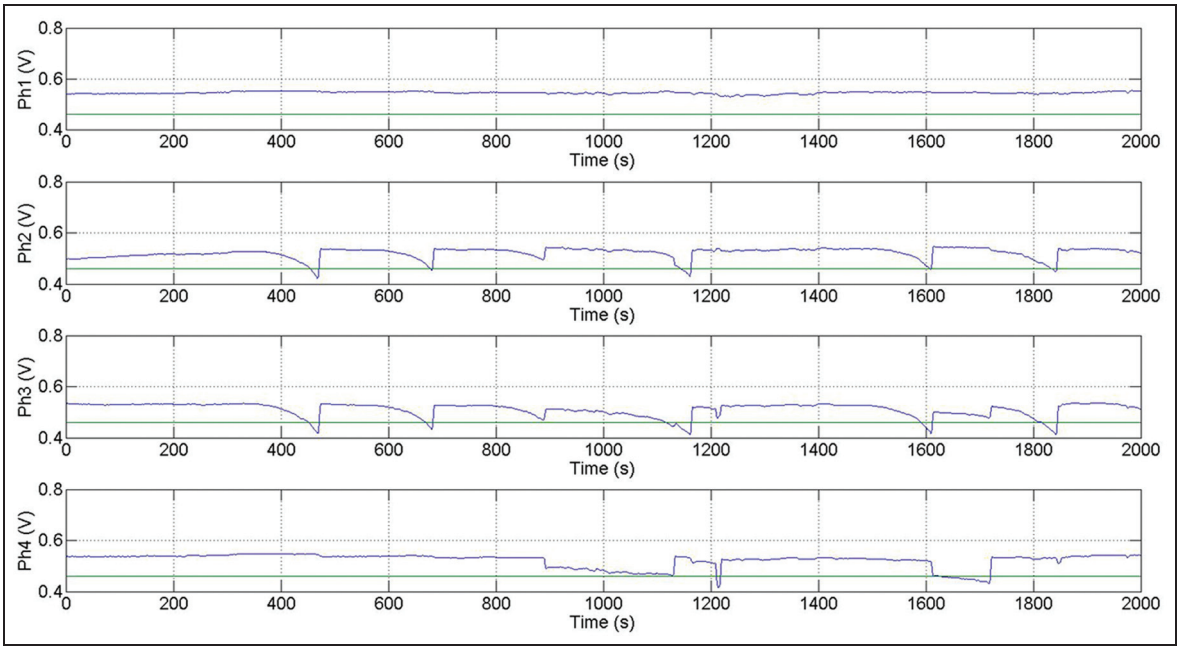

Figure 15. Time history of the signal from photodiodes.

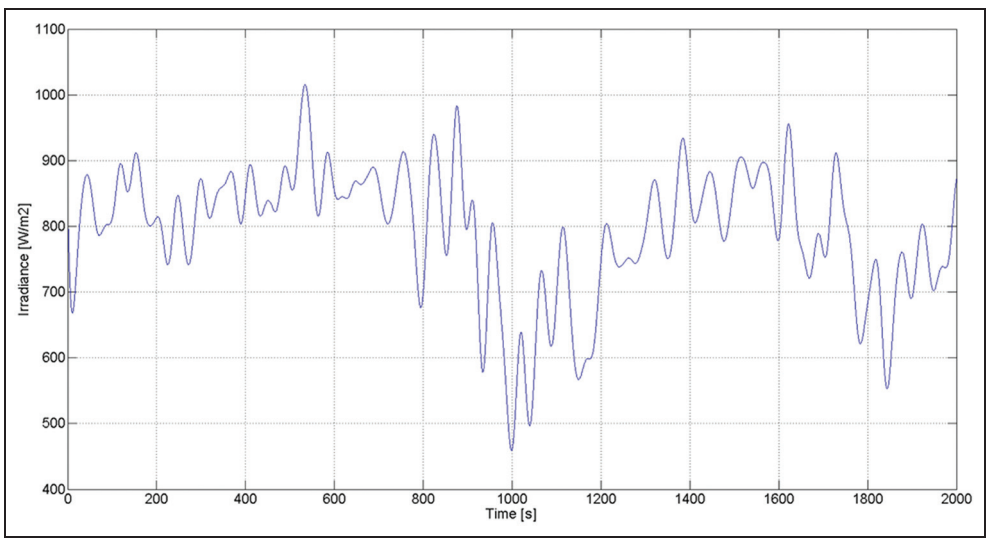

Figure 16. Irradiance measured using the screened pyranometer.

static phases, during which the orientation error is within the acceptance limit and all the photodiodes are enlightened, and alignment phases, starting when the signals from at least a photodiode falls under the activation threshold. In these last phases, the machine moves and the photodiode signals rise again until the activation threshold is overcome. Other less relevant data about testing are reported in Mauro and Scarzella.[27] Figure 15 makes it possible to understand that the controlled mechanism fully performs sun tracking. The complete lighting of all four photodiodes is reached for the 99% of the test time.

Finally, Figure 16 shows the data measured by the screened pyranometer. The instrument provides a signal which is proportional to irradiance when it is oriented toward the sun with an alignment error lower than 0.4°. The chart in the figure points out that the alignment with the sun direction was constantly maintained within the sensor acceptance angle, as the measured irradiance never falls to 0. The variation in the irradiance values is due to light clouds projecting their shadows on the test site during some moments of test and to environmental electrical disturbance that could not be removed.

Downloaded from ade.sagepub.com at Politecnico di Torino on December 9, 2015

Conclusion

In this work, a suitable solution was found to obtain a workspace that fits the requirements for sun tracking with a parallel kinematics mechanism. The kinematic analysis was carried in order to exclude the presence of any kind of singularity within the workspace. According to this finding, a small-scale prototype was developed, including mechanical hardware and control system. After the setup, the prototype was tested in an outdoor environment to verify the capability of aligning the plane of the photovoltaic modules normally to the sun keeping the misalignment within the requirement imposed for the use of high-concentration photovoltaic modules. Energetic analysis leads to the conclusion that the energy consumption of the mover can be neglected with respect to the energy produced by a 0.36-m^2, or 108-W_p, concentration module driven by the prototype.

The results showed a satisfactory behavior of the proposed system as it proved itself to be able to provide orientation of the photovoltaic module within the strict requirements of high-concentration photovoltaic systems together with a low energy consumption. The alignment error was indeed always maintained under 0.4° as no discontinuity in the irradiance measured by a masked pyranometer was found. This result was obtained due to the efficiency of the embedded control system and to the high stiffness of the mechanism. The external action that should be exerted on the platform to induce significant displacements of the end-effector is much higher than the one that could be applied by wind. A full-scale prototype was built after the results from tests on this system and energy productivity tests are running now. The results of these tests will be described in a future work when they will be disposable.

Acknowledgements

The authors wish to thank Edward Johnston for his help in the final revision of this article.

Declaration of conflicting interests

The author(s) declared no potential conflicts of interest with respect to the research, authorship, and/or publication of this article.

Funding

The author(s) disclosed receipt of the following financial support for the research, authorship, and/or publication of this article: The authors thank Regione Piemonte—Polo di Innovazione Polight—for the support provided to this research within the SOLARBUILD project, POR-FESR program 2007–2014.

References

1. Chin CS, Babu A and McBride W. Design, modeling and testing of a standalone single axis active solar tracker using MATLAB/Simulink. *Renew Energ* 2011; 36: 3075–3090.
2. Cotal H, Fetzer C, Boisvert J, et al. III–V multijunction solar cells for concentrating photovoltaics. *Energ Environ Sci* 2009; 2: 174–192.
3. King RR, Bhusari D, Larrabee D, et al. Solar cell generations over 40% efficiency. *Prog Photovoltaics* 2012; 10: 801–815.
4. Zubi G, Bernal-Augustín JL and Fracastoro GV. High concentration photovoltaic systems applying III–V cells. *Renew Sust Energ Rev* 2009; 13: 2646–2652.
5. Peharz G and Dimroth F. Energy payback time of the high-concentration PV systems FLATCON®. *Prog Photovoltaics* 2005; 13: 627–634.
6. Nishioka K, Takamoto T, Agui T, et al. Annual output estimation of concentrator photovoltaic systems using high-efficiency InGaP/InGaAs/Ge triple-junction solar cells based on experimental solar cell's characteristics and field-test meteorological data. *Sol Energ Mat Sol C* 2006; 90: 57–67.
7. Roth P, Georgiev A and Boudinov H. Design and construction of a system for sun-tracking. *Renew Energ* 2004; 29: 393–402.
8. Mousazadeh H, Keyhani A, Javadi A, et al. A review of principle and sun-tracking methods for maximizing solar systems output. *Renew Sust Energ Rev* 2009; 13: 1800–1818.
9. Itul T and Pisla D. Dynamics of a 3-DOF parallel mechanism used for orientation applications. In: *Proceedings of the IEEE international conference on automation, quality and testing, robotics* (AQRT 2008—THETA 16th edition, Cluj-Napoca, 22–25 May 2008, vol. 2, pp.398–403. New York, NY: IEEE.
10. Kulkarni S, Tonapi S and Larochelle P. Effect of tracking flat reflector using novel auxiliary drive mechanism on the performance of stationary photovoltaic module. In: *Proceedings of IMECE2007 ASME international mechanical engineering congress and exposition*, Seattle, WA, 11–15 November 2007, vol. 6, pp.351–356. New York, NY: ASME.
11. Levy SL. High (500x) concentration PV array conceptual design. In: *Proceedings of the 15th IEEE photovoltaic specialists conference*, Orlando, FL, 1 May 1984. New York, NY: IEEE.
12. Li W, Sun J, Zhang J, et al. A novel parallel 2-DOF spherical mechanism with one-to-one input-output mapping. In: *Proceedings of the 6th WSEAS international conference on robotics, control and manufacturing technology*, Hangzhou, China, 16–18 April 2006, pp.6–11. WSEAS.
13. Ferraresi C, Pastorelli S, Sorli M, et al. Static and dynamic behavior of a high stiffness Stewart platform-based force/torque sensor. *J Robotic Syst* 1995; 12: 883–893.
14. Gosselin CM. Stiffness mapping for parallel manipulators. *IEEE T Robotic Autom* 1990; 6: 377–382.
15. Huang T, Zhao X and Whitehouse DJ. Stiffness estimation of a tripod-based parallel kinematic machine. *IEEE T Robotic Autom* 2002; 18: 50–58.

Downloaded from ade.sagepub.com at Politecnico di Torino on December 9, 2015

16. Dong W, Sun LN and Du ZJ. Design of a precision compliant parallel positioner driven by dual piezoelectric actuators. *Sensor Actuat A: Phys* 2007; 135: 205–256.
17. Cammarata A. Optimized design of a large-workspace 2-DOF parallel robot for solar tracking systems. *Mech Mach Theory* 2015; 83: 175–186.
18. Alexandru C and Pozna C. Simulation of a dual-axis solar tracker for improving the performance of a photovoltaic panel. *Proc IMechE, Part A: J Power and Energy* 2010; 224: 797–811.
19. Altuzarra O, Macho E, Aginaga J, et al. Design of a solar tracking parallel mechanism with low energy consumption. *Proc IMechE, Part C: J Mechanical Engineering Science* 2014; 229: 566–579.
20. Neugebauer R, Schwaar M, Ihlenfeldt S, et al. New approaches to machine structures to overcome the limits of classical parallel structures. *CIRP Ann: Manuf Techn* 2002; 51: 293–296.
21. Yu D. Kinematic calibration of a parallel robot using coordinate measuring machine. *Int J Phys Sci* 2011; 6: 4999–5004.
22. Dunlop GR and Jones TP. Position analysis of a two DOF parallel mechanism—the Canterbury tracker. *Mech Mach Theory* 1999; 34: 599–614.
23. Zeroual A, Mustapha R, Ankrim M, et al. Design and construction of a closed loop sun-tracker with microprocessor management. *Int J Sol Energ* 1998; 19: 263–274.
24. Mauro S and Scarzella C. Parallel mechanism for precision sun tracking. In: *Proceeding of the ASME 2010, 10th biennial conference on engineering system design and analysis*, Istanbul, 12–14 July 2010, pp.17–22. New York: ASME.
25. Tsai L-W. *Robot analysis: the mechanics of serial and parallel manipulators*. New York: John Wiley & Sons, 1999.
26. Zlatanov D, Bonev IA and Gosselin CM. Constraint singularities of parallel mechanisms. In: *Proceedings of the ICRA'02 IEEE international conference on robotics and automation*, Washington, DC, 11–15 May 2002, vol. 1. New York: IEEE.
27. Mauro S and Scarzella C. Developing a parallel kinematic suntracker for HCPV. In: *Proceeding of ASME 2012, 11th biennial conference on engineering system design and analysis*, Nantes, 2–4 July 2012, pp.459–464. New York: ASME.

Downloaded from ade.sagepub.com at Politecnico di Torino on December 9, 2015